GEOPHYSICS, VOL. 82, NO. 3 (MAY-JUNE 2017); P. F15–F28, 11 FIGS.
10.1190/GEO2016-0397.1

Perturbational and nonperturbational inversion of Rayleigh-wave velocities

Matthew M. Haney[1] and Victor C. Tsai[2]

ABSTRACT

The inversion of Rayleigh-wave dispersion curves is a classic geophysical inverse problem. We have developed a set of MATLAB codes that performs forward modeling and inversion of Rayleigh-wave phase or group velocity measurements. We describe two different methods of inversion: a perturbational method based on finite elements and a nonperturbational method based on the recently developed Dix-type relation for Rayleigh waves. In practice, the nonperturbational method can be used to provide a good starting model that can be iteratively improved with the perturbational method. Although the perturbational method is well-known, we solve the forward problem using an eigenvalue/eigenvector solver instead of the conventional approach of root finding. Features of the codes include the ability to handle any mix of phase or group velocity measurements, combinations of modes of any order, the presence of a surface water layer, computation of partial derivatives due to changes in material properties and layer boundaries, and the implementation of an automatic grid of layers that is optimally suited for the depth sensitivity of Rayleigh waves.

INTRODUCTION

Inferring shear wave velocity profiles from Rayleigh wave dispersion curves is a problem in seismology with a long history (Dorman and Ewing, 1962; Aki and Richards, 1980). Dispersion curve inversion remains a robust and powerful tool for practicing seismologists to characterize the subsurface (Xia et al., 1999), and there continues to be a need for codes to perform Rayleigh-wave inversion (Cercato, 2007, 2008; Garofalo et al., 2016). Ambient noise seismology uses such an inversion because the ambient seismic field is typically dominated by fundamental-mode surface waves (Gerstoft et al., 2006; Brenguier et al., 2007). Ambient noise at the ocean floor is similarly composed of a type of surface wave known as the Scholte wave (Muyzert, 2007). The wavefield radiated by volcanic tremor is in many cases also made up of surface waves, whose dispersive properties can be used to invert for volcanic structure when measured on a small aperture array (Chouet et al., 1998; Saccorotti et al., 2003).

To determine a 1D shear velocity structure given measured Rayleigh-wave velocities as a function of frequency, one must first be able to solve the forward problem of computing Rayleigh-wave velocities and mode shapes given a 1D structural model. Many techniques have been developed to solve the forward problem for Rayleigh waves (Aki and Richards, 1980). The conventional method is based on the Thomson-Haskell recursion formula and reduces the problem to finding the roots of a polynomial, i.e., when the value of a matrix determinant is zero (Takeuchi and Saito, 1972; Saito, 1988). Once the root is found, the mode shape can be computed because the model is assumed to consist of a stack of homogeneous layers. In this paper, we focus on an alternative finite-element method of solving for wave velocities and mode shapes of Rayleigh waves. This approach originates from a paper by Lysmer (1970), and is known as the thin-layer method (Kausel, 2005) because the individual finite elements, or layers, must be thin compared with the wavelength to ensure accuracy. In contrast to the conventional method, this finite-element method leads to a generalized eigenvalue/eigenvector problem:

$$\mathbf{A}\mathbf{x} = \gamma\mathbf{B}\mathbf{x}, \tag{1}$$

where $\mathbf{A}$ and $\mathbf{B}$ are banded matrices. In this formulation, the Rayleigh-wave phase velocity is related to the eigenvalue γ and the shape of the mode in depth is the eigenvector $\mathbf{x}$. The solution of equation 1 is not trivial. Fortunately, many available codes exist for solving equation 1 for a given number of the smallest (or largest) eigenvalues and their associated eigenvectors. Thus, the forward problem for Rayleigh waves reduces to simply setting up a linear system of the form of equation 1 and solving it with established numerical codes. As pointed out by Lysmer (1970), this approach is much simpler than other methods for modeling Rayleigh waves. Other researchers have

Peer-reviewed code related to this article can be found at http://software.seg.org/2017/0003.
Manuscript received by the Editor 27 July 2016; published online 03 April 2017.
[1]U.S. Geological Survey Volcano Science Center, Alaska Volcano Observatory, Anchorage, Alaska, USA. E-mail: mhaney@usgs.gov.
[2]California Institute of Technology, Seismological Laboratory, Pasadena, California, USA. E-mail: tsai@caltech.edu.

modeled normal modes and guided waves with similar techniques. For example, Wiggins (1976) models the normal modes of the earth with a finite-element method using an eigenvalue/eigenvector solver. Aki and Richards (1980) briefly describe a closely related Rayleigh-Ritz technique for modeling Rayleigh waves. A similar approach has also been described by Karpfinger et al. (2010) for the forward modeling of guided waves in a borehole.

The original work by Lysmer (1970) only deals with the forward problem. Kausel (2005) briefly touches on the use of the finite-element method for nondestructive testing and inversion. In this paper, we develop the method further to address the inverse problem of obtaining depth models from dispersion curves. Because the finite-element method leads to a matrix formulation of the forward problem, a clear link can be made to the inverse problem using matrix perturbation theory. By optimizing the use of an eigensolver, Rayleigh waves can be modeled quickly and an iterative inversion is possible. Although the basic principles of Rayleigh-wave inversion based on perturbation theory are well-known (Aki and Richards, 1980), it is presented here in matrix-vector notation instead of a continuous formulation. The matrix-vector notation is particularly well-suited for the development of computer programs. The extension of the method to inversion leads to a set of MATLAB codes that can invert any collection of phase or group velocity measurements of any modes (fundamental, first higher mode, etc.) for a shear-wave depth profile. The codes include three examples of phase velocity inversion — two at a crustal scale and the other in a near-surface setting. The two crustal-scale examples involve higher modes and the presence of a water layer on top of the model.

To complement the perturbational inversion codes, we also delve into the issue of constructing an accurate initial model. We use a nonperturbational type of Rayleigh-wave inversion recently introduced by Haney and Tsai (2015) that bears similarities to the Dix equation in reflection seismology. In one of the software examples included with this paper, we show how to use the Dix-type relation from Haney and Tsai (2015) to construct an initial model for noisy synthetic data from the near-surface MODX model (Xia et al., 1999). The initial model is then further refined using iterative perturbational inversion until a final model is found that fits the synthetic data to within the noise level.

FORWARD MODELING OF RAYLEIGH DISPERSION

The application of the finite-element method for forward modeling surface waves has been exhaustively described by Lysmer (1970) and Kausel (2005). In this section, we do not rederive the method but discuss its salient points. We approximate Rayleigh-wave eigenfunctions by linear finite elements and represent subsurface material properties with thin homogeneous layers described by boxcar functions. Figure 1 shows these linear and boxcar functions graphically. Thus, the eigenfunctions are parameterized at the nodes and the material properties apply to the elements between the nodes. Note that there are N elements and $N+1$ nodes in the 1D finite-element mesh. However, the deepest node at z_{N+1} is fixed to be zero. The crux of the finite-element method for modeling Rayleigh-wave eigenfunctions is that the base of the model is sufficiently deep such that having the deepest node set to zero is effectively the same as the eigenfunction decaying exponentially to zero at infinite depth. This is also known as the locked-mode approximation (Nolet et al., 1989), and later we will quantify what we mean by the deepest node being deep enough to approximate a half-space.

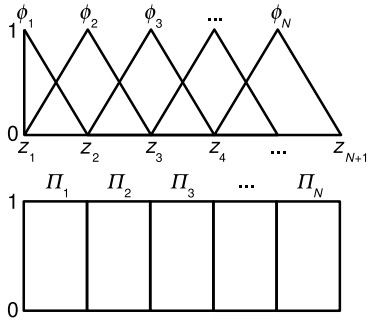

Figure 1. The linear and boxcar basis functions used for discretizing the Rayleigh-wave eigenfunctions (linear) and material properties (boxcar) in the finite-element method of Lysmer (1970).

We organize the N unknown nodal displacements with alternating horizontal eigenfunction (r_1) and vertical eigenfunction (r_2) components as

$$\mathbf{v} = [\ \ldots \quad r_1^{K-1} \quad r_2^{K-1} \quad r_1^{K} \quad r_2^{K} \quad r_1^{K+1} \quad r_2^{K+1} \quad \ldots\ ]^T, \tag{2}$$

where K is an index. With this organization, the complete Rayleigh-wave eigenvector is given by a generalized quadratic eigenvalue problem in terms of the wavenumber k

$$(k^2\mathbf{B}_2 + k\mathbf{B}_1 + \mathbf{B}_0)\mathbf{v} = \omega^2\mathbf{M}\mathbf{v}. \tag{3}$$

The stiffness matrices $\mathbf{B}_2$, $\mathbf{B}_1$, and $\mathbf{B}_0$ are only dependent on Lamé's first parameter λ and shear modulus μ, whereas the mass matrix $\mathbf{M}$ only depends on density ρ. All four of the matrices are real-valued and symmetric (Lysmer, 1970), a property that takes on an important role in the development of the inverse problem. The matrices $\mathbf{B}_2$, $\mathbf{B}_1$, $\mathbf{B}_0$, and $\mathbf{M}$ are discussed in detail by Kausel (2005), and they are described briefly in Appendix A for completeness.

Although equation 3 could be solved as a generalized linear eigenvalue problem in terms of squared frequency for a known wavenumber k, Rayleigh-wave properties in seismology are typically needed at a given frequency, with k being the unknown eigenvalue. This makes solving the quadratic eigenvalue problem in terms of k necessary. By defining an auxiliary variable $\mathbf{a} = k\mathbf{v}$, equation 3 can be rewritten as

$$k\mathbf{B}_2\mathbf{a} = \omega^2\mathbf{M}\mathbf{v} - \mathbf{B}_1\mathbf{a} - \mathbf{B}_0\mathbf{v}. \tag{4}$$

This equation together with $\mathbf{a} = k\mathbf{v}$ gives the generalized linear eigenvalue problem:

$$k\begin{bmatrix}\mathbf{I} & 0\\ 0 & \mathbf{B}_2\end{bmatrix}\begin{bmatrix}\mathbf{v}\\ \mathbf{a}\end{bmatrix} = \begin{bmatrix}0 & \mathbf{I}\\ \omega^2\mathbf{M}-\mathbf{B}_0 & -\mathbf{B}_1\end{bmatrix}\begin{bmatrix}\mathbf{v}\\ \mathbf{a}\end{bmatrix}. \tag{5}$$

Note that the introduction of the auxiliary variable $\mathbf{a}$ doubles the size of the eigenvectors. Once equation 5 has been solved for the eigenvalue and eigenvector corresponding to a given mode, the group velocity U can be calculated as

$$U = \frac{\delta\omega}{\delta k} = \frac{\mathbf{v}^T(2k\mathbf{B}_2 + \mathbf{B}_1)\mathbf{v}}{2\omega\mathbf{v}^T\mathbf{M}\mathbf{v}}, \tag{6}$$

as derived in Appendix B. Although not shown in the above equations, we can also allow for a water layer on the top of the model. Appendix C discusses how the above equations change in the presence of a water layer.

Finding the eigenvalue and eigenvector of a given mode poses a significant challenge. For a fixed frequency, the fundamental mode corresponds to the largest eigenvalue in equation 5. This can be seen from the relation $k = \omega/c$: The fundamental mode has the lowest phase velocity and thus the largest value of k. One approach for a finite-element grid with N nodes would be to solve for all $2N$ eigenvalues and eigenvectors of equation 5 and search for the largest eigenvalue. There are $2N$ eigenvalues/eigenvectors because the system is augmented with the auxiliary variable $\mathbf{a}$. In the interest of computational speed, it would be ideal if the eigenvalue/eigenvector solver could instead be asked to only find the modes of interest, whether fundamental or higher modes. In MATLAB, this can be accomplished using the function eigs, a solver based on the ARPACK linear solver (Lehoucq et al., 1998). This solver can find an eigenvalue (or group of eigenvalues) closest to a particular value. Because the fundamental mode corresponds to the largest k eigenvalue, this feature can be used once an upper bound on the fundamental mode eigenvalue is known.

We obtain the upper bound on the fundamental mode eigenvalue in the following way. We consider different half-spaces, with velocities determined by a given node's velocities, and compute half-space Rayleigh-wave velocities for each of the nodes. We then select the minimum value, c_{low}, and this gives an upper bound on the wavenumber, $k_{\text{up}} = \omega/c_{\text{low}}$. Asking the eigensolver to find the closest eigenvalue/eigenvector to this upper bound results in the eigensolver returning the fundamental mode. Similarly, asking the eigensolver to find the two closest eigenvalues/eigenvectors to this upper bound results in the eigensolver returning the fundamental mode and the first higher mode. Note that, with this approach, we cannot compute the first higher mode without also computing the fundamental mode. However, this approach offers a significant speed-up compared with finding the modes of interest among all calculated eigenvalues. Such a speed-up is important given that the calculation of the eigenvalues/eigenvectors is the main workhorse for the inverse problem. In Appendix C, we briefly discuss how to find an upper bound on the eigenvalue when a water layer exists on top of an elastic medium.

A key consideration for forward modeling is accuracy and, for this, an important concept is the depth sensitivity of Rayleigh waves. Xia et al. (1999) conduct numerical tests and find the Rayleigh-wave maximum sensitivity depth to be well-described by 0.63ℓ, where ℓ is the wavelength. Haney and Tsai (2015) further show that, although sensitivity is spread out among all depths, a good rule of thumb in vertically inhomogeneous velocity profiles is that the fundamental mode Rayleigh wave is sensitive to a depth of approximately 0.5ℓ. This concept can be generalized to higher modes by taking the deepest sensitivity as $0.5m\ell$, where m is the mode number and $m = 1$ is the fundamental mode, $m = 2$ is the first overtone, and so on. With the sensitivity depth in mind, there are two factors that control the accuracy of the finite-element method: the depth of the model L and the thickness of the elements h_k. The model must be sufficiently deep so that the Dirichlet boundary condition at the base of the model is a good approximation of the vanishing condition at infinite depth. This requires that the eigenvector of the mode be small at this depth. One way to ensure this is to require the depth of the model be at least twice the depth of maximum sensitivity at a certain frequency:

$$L > m\ell. \tag{7}$$

Regarding the thickness of the elements, the principle guiding accuracy is simply one of sufficiently sampling the eigenvector, similar to dispersion considerations for time-domain wave-propagation algorithms (Marfurt, 1984). We require the wavelength to be greater than five times the element thickness at all depths above the depth of maximum sensitivity:

$$\ell > 5h_s, \tag{8}$$

where h_s is the element thickness at all depths above the maximum sensitivity depth ($z = 0.5m\ell$). This means that Rayleigh waves are well-sampled down to their sensitivity depth, but below that depth they are under-sampled in the model. However, the under-sampling is not an issue because below the maximum sensitivity depth, the Rayleigh-wave eigenfunction is a smoothly decaying exponential. If either of the inequalities in equations 7 and 8 are not satisfied in the forward modeling code that we show in the "Software Examples" section, then the code outputs an error message and asks the user to either extend the model in depth or densify the finite-element grid. Based on sensitivity depth considerations, we derive in Appendix D an optimal type of nonuniform finite-element grid of layers for Rayleigh waves.

The final question in forward modeling is whether a guided mode exists or not at a particular frequency in a certain depth model. For example, Rayleigh overtones do not exist for a homogeneous model. To address whether a mode exists, we analyze the vertical component of the eigenvector and insist that its absolute value decay more quickly than a linearly decreasing function between the surface and the base of the model, in which the mode is fixed to be zero. The depth integral of a linearly decreasing function over the top half of the model is three times larger than the integral over the bottom half of the model when the linearly decreasing function goes to zero at the base. Therefore, if the ratio of the depth integral over the top half of the model to the depth integral over the bottom half of the model is less than three, we classify the mode as nonguided. A mode that is not guided oscillates in depth and does not exponentially decay, so this criterion effectively detects whether an eigenvector decays quickly enough with depth to be considered guided. In the codes described in a later section, the forward modeling code returns NaNs for Rayleigh-wave velocities and mode shapes when the mode is nonguided. The subsequent functions detect the NaNs and do not include measurements made for those mode/frequency pairs in the inversion.

PERTURBATIONAL INVERSION OF DISPERSION CURVES

Although Lysmer (1970) fully addresses the forward modeling of Rayleigh waves, the inverse problem was not investigated. Here, we extend the finite-element method to include inversion as well. The matrix-vector formulation of the forward problem in the previous section is well-suited for developing the inversion using straightforward perturbation theory. As shown in Appendix E, the perturbation in phase velocity due to perturbations in the material properties at fixed frequency is given by

$$\frac{\delta c}{c} = \frac{1}{2k^2 U c \mathbf{v}^T \mathbf{M} \mathbf{v}} \left(\sum_{i=1}^{N} \mathbf{v}^T \frac{\partial (k^2 \mathbf{B}_2 + k\mathbf{B}_1 + \mathbf{B}_0)}{\partial \mu_i} \mathbf{v} \delta \mu_i + \sum_{i=1}^{N} \mathbf{v}^T \frac{\partial (k^2 \mathbf{B}_2 + k\mathbf{B}_1 + \mathbf{B}_0)}{\partial \lambda_i} \mathbf{v} \delta \lambda_i - \omega^2 \sum_{i=1}^{N} \mathbf{v}^T \frac{\partial \mathbf{M}}{\partial \rho_i} \mathbf{v} \delta \rho_i \right). \quad (9)$$

Note that the eigenvector $\mathbf{v}$, wavenumber k, phase speed c, and group speed U all correspond to the mode of interest; thus, equation 9 applies individually to all modes including higher modes. The matrices appearing in equation 9 are the same as those in the forward problem (equation 3). Thus, the connection between the forward and inverse problem is clear using the matrix-vector notation. Equation 9 is the discrete version of the continuous relations found in Aki and Richards (1980). The derivatives of matrices with respect to the material properties shown above are extremely sparse, and so any matrix-vector multiplications involving these matrices have been hard-coded in the associated programs for best computational speed.

Evaluated over many frequencies, the above equation results in a linear matrix-vector relation between the perturbed phase velocities and the perturbations in material properties:

$$\frac{\boldsymbol{\delta c}}{\mathbf{c}} = \mathbf{K}_\mu^c \frac{\boldsymbol{\delta \mu}}{\boldsymbol{\mu}} + \mathbf{K}_\lambda^c \frac{\boldsymbol{\delta \lambda}}{\boldsymbol{\lambda}} + \mathbf{K}_\rho^c \frac{\boldsymbol{\delta \rho}}{\boldsymbol{\rho}}, \quad (10)$$

where $\mathbf{K}_\mu^c$, $\mathbf{K}_\lambda^c$, and $\mathbf{K}_\rho^c$ are the phase-velocity kernels for shear modulus, Lamé's first parameter, and density, respectively. Note that the kernels shown here are for relative perturbations in the phase velocities and material properties.

Although equation 10 is a linear relation between phase-velocity perturbations and perturbations in all three material properties, Rayleigh-wave phase and group velocities are typically only inverted for depth-dependent shear-wave velocity profiles in practice. This is because Rayleigh-wave velocities are most dependent on shear-wave velocity in the subsurface (Xia et al., 1999). In the associated inversion codes, we have implemented two ways to express equation 10 in terms of shear velocity only, by assuming that (1) Poisson's ratio and density are fixed throughout the inversion or (2) P-wave velocity and density are fixed.

To find the linear relation between phase velocity perturbations and shear-wave velocity for the first case of fixed Poisson's ratio and density, we use the following relations valid to first order:

$$\frac{\delta \mu}{\mu} = 2\frac{\delta \beta}{\beta} + \frac{\delta \rho}{\rho}, \quad (11)$$

and

$$\frac{\delta \lambda}{\lambda} = \left(\frac{2\alpha^2}{\alpha^2 - 2\beta^2} \right) \frac{\delta \alpha}{\alpha} - \left(\frac{4\beta^2}{\alpha^2 - 2\beta^2} \right) \frac{\delta \beta}{\beta} + \frac{\delta \rho}{\rho}, \quad (12)$$

where α is the compressional-wave velocity and β is the shear-wave velocity. A fixed Poisson's ratio implies a constant ratio of $\alpha/\beta = R$ in the subsurface, and in this case, equation 12 can be written as

$$\frac{\delta \lambda}{\lambda} = \left(\frac{2R^2}{R^2 - 2} \right) \frac{\delta \alpha}{\alpha} - \left(\frac{4}{R^2 - 2} \right) \frac{\delta \beta}{\beta} + \frac{\delta \rho}{\rho}. \quad (13)$$

A constant value of R also implies that the relative perturbations in the wave speeds are the same: $\delta\alpha/\alpha = \delta\beta/\beta$. Thus, equation 13 can be reduced to

$$\frac{\delta \lambda}{\lambda} = 2\frac{\delta \beta}{\beta} + \frac{\delta \rho}{\rho}, \quad (14)$$

which is the same as equation 11 and shows that for a medium with a constant R, the relative perturbations in the two moduli are the same. Substituting equations 11 and 14 into equation 10 gives

$$\frac{\boldsymbol{\delta c}}{\mathbf{c}} = 2(\mathbf{K}_\mu^c + \mathbf{K}_\lambda^c) \frac{\boldsymbol{\delta \beta}}{\boldsymbol{\beta}} + (\mathbf{K}_\mu^c + \mathbf{K}_\lambda^c + \mathbf{K}_\rho^c) \frac{\boldsymbol{\delta \rho}}{\boldsymbol{\rho}}. \quad (15)$$

Finally, by assuming no perturbations in the density model, this yields

$$\frac{\boldsymbol{\delta c}}{\mathbf{c}} = 2(\mathbf{K}_\mu^c + \mathbf{K}_\lambda^c) \frac{\boldsymbol{\delta \beta}}{\boldsymbol{\beta}} = \mathbf{K}_\beta^{c,R} \frac{\boldsymbol{\delta \beta}}{\boldsymbol{\beta}}. \quad (16)$$

In this case, the shear-wave velocity kernel is twice the sum of the λ and μ kernels.

For the other case of fixed P-wave velocity and density, we first write equations 11 and 12 in matrix vector form as

$$\frac{\boldsymbol{\delta \mu}}{\boldsymbol{\mu}} = 2\frac{\boldsymbol{\delta \beta}}{\boldsymbol{\beta}} + \frac{\boldsymbol{\delta \rho}}{\boldsymbol{\rho}}, \quad (17)$$

and

$$\frac{\boldsymbol{\delta \lambda}}{\boldsymbol{\lambda}} = \mathbf{D}_1 \frac{\boldsymbol{\delta \alpha}}{\boldsymbol{\alpha}} - \mathbf{D}_2 \frac{\boldsymbol{\delta \beta}}{\boldsymbol{\beta}} + \frac{\boldsymbol{\delta \rho}}{\boldsymbol{\rho}}, \quad (18)$$

where $\mathbf{D}_1$ and $\mathbf{D}_2$ are the matrices whose only nonzero elements lie on the main diagonal and are given by the quantities shown in equation 12. Substituting equations 17 and 18 into equation 10 and setting perturbations in P-wave velocity and density to zero gives

$$\frac{\boldsymbol{\delta c}}{\mathbf{c}} = [2\mathbf{K}_\mu^c - \mathbf{K}_\lambda^c \mathbf{D}_2] \frac{\boldsymbol{\delta \beta}}{\boldsymbol{\beta}} = \mathbf{K}_\beta^{c,\alpha} \frac{\boldsymbol{\delta \beta}}{\boldsymbol{\beta}}, \quad (19)$$

which is the linear relation between phase velocity and shear-wave velocity, under the assumption of no perturbations in P-wave velocity and density. In this case, the shear-wave velocity kernel is a weighted sum of the λ and μ kernels.

Whichever case is chosen for relating phase velocity perturbations and perturbations in shear velocity, equation 16 for $\mathbf{K}_\beta^{c,R}$ or 19 for $\mathbf{K}_\beta^{c,\alpha}$ defines the shear-wave phase velocity kernel $\mathbf{K}_\beta^c$. It turns out that the sensitivity kernel for group velocities is related to the phase-velocity kernel (Rodi et al., 1975) as

$$\mathbf{K}_\beta^U = \mathbf{K}_\beta^c + \frac{U\omega}{c} \frac{\partial \mathbf{K}_\beta^c}{\partial \omega}. \quad (20)$$

In the numerical codes described later, the derivative of the phase velocity kernel with respect to frequency in equation 20 is evaluated numerically using second-order-accurate differencing. A similar

linear relation as in equation 16 or 19 can thus be set up for group velocity

$$\frac{\delta \mathbf{U}}{\mathbf{U}} = \mathbf{K}_{\beta}^{U} \frac{\delta \boldsymbol{\beta}}{\boldsymbol{\beta}}. \tag{21}$$

This equation is the basis for perturbational group velocity inversion. In the numerical codes, the linear relations shown in equations 16, 19, and 21 are set up in terms of absolute perturbations instead of relative perturbations. Denoting the group velocity kernel in this case as $\mathbf{G}_{\beta}^{U}$, the absolute perturbation kernel can be given in terms of the relative perturbation kernel as

$$\mathbf{G}_{\beta}^{U} = \mathrm{diag}(\mathbf{U})\mathbf{K}_{\beta}^{U}\mathrm{diag}(\boldsymbol{\beta})^{-1}, \tag{22}$$

where $\mathrm{diag}(\mathbf{U})$ is a matrix with the vector $\mathbf{U}$ placed on the main diagonal and off-diagonal entries equal zero. The same form applies to the computation of absolute phase velocity kernels from the relative kernels.

Inversion of phase or group velocities requires adopting a type of regularization. Here, we describe a simple method based on weighted-damped least squares. Data covariance and model covariance matrices, $\mathbf{C}_d$ and $\mathbf{C}_m$, are chosen as in Gerstoft et al. (2006). The data covariance matrix is assumed to be a diagonal matrix:

$$\mathbf{C}_d(i,i) = \sigma_d(i)^2, \tag{23}$$

where $\sigma_d(i)$ is the data standard deviation of the ith phase or group velocity measurement. The model covariance matrix has the form,

$$\mathbf{C}_m(i,j) = \sigma_m^2 \exp(-|z_i - z_j|/d), \tag{24}$$

where σ_m is the model standard deviation, z_i and z_j are the depths at the top of the ith and jth elements, and d is a smoothing distance or correlation length. In the numerical codes, the model standard deviation is given as a user-supplied factor times the median of the data standard deviations.

With the covariance matrices so chosen, phase/group velocity inversion proceeds using the algorithm of total inversion (Tarantola and Valette, 1982; Muyzert, 2007). We denote the kernel $\mathbf{G}_{\beta}$ because in general it may reflect phase and group velocity measurements. The nth model update $\boldsymbol{\beta}_n$ is calculated by forming the augmented system of equations (Snieder and Trampert, 1999; Aster et al., 2004) based on the algorithm of total inversion (Tarantola and Valette, 1982; Muyzert, 2007):

$$\begin{bmatrix} \mathbf{C}_d^{-1/2} \\ 0 \end{bmatrix} (\mathbf{U}_0 - \mathbf{f}(\boldsymbol{\beta}_{n-1}) + \mathbf{G}_{\beta}(\boldsymbol{\beta}_{n-1} - \boldsymbol{\beta}_0)) = \begin{bmatrix} \mathbf{C}_d^{-1/2}\mathbf{G}_{\beta} \\ \mathbf{C}_m^{-1/2} \end{bmatrix} (\boldsymbol{\beta}_n - \boldsymbol{\beta}_0), \tag{25}$$

where $\mathbf{U}_0$ is the phase/group velocity data, $\mathbf{f}$ is the (nonlinear) forward modeling operator, and n ranges from one to whenever the stopping criterion is met or the maximum allowed number of iterations is reached. The stopping criterion used here is based on the chi-squared value (Gouveia and Scales, 1998)

$$\chi^2 = (\mathbf{f}(\boldsymbol{\beta}_n) - \mathbf{U}_0)^T \mathbf{C}_d^{-1} (\mathbf{f}(\boldsymbol{\beta}_n) - \mathbf{U}_0)/F, \tag{26}$$

where F is the number of measurements (the number of Rayleigh phase/group velocity measurements). The iteration is terminated when the χ^2 value falls within a user-prescribed window. In the code examples shown later, this window is set for χ^2 between 1 and 1.5. The augmented matrix-vector relation can be passed to a conjugate gradient solver (Paige and Saunders, 1982). The inversion given in equation 25 is then iterated to convergence, except for the case in which the maximum allowed number of iterations is reached. Note that, in the iteration, if an updated model increases the chi-squared valued from the previous model, the length of the gradient step between the previous model and the potential update is scaled down by a factor of one-half. This is called a reduction step, and it is repeated until the chi squared of the update is less than the previous model or the maximum allowed number of reduction steps is reached. Including reduction steps in the algorithm through this simple line search increases convergence substantially.

NONPERTURBATIONAL INVERSION OF DISPERSION CURVES

The perturbational inversion we described in the previous section is effective at refining an initial model of shear-wave velocity; however, the issue of creating an acceptable initial model remains. Recently, Haney and Tsai (2015) show that, to a good approximation, a linear matrix-vector relationship exists between the squared phase velocities and the squared shear velocities for a set of layers:

$$\mathbf{c}^2 = \mathbf{G}\boldsymbol{\beta}^2, \tag{27}$$

where $\mathbf{G}$ is the kernel relating squared shear velocities to squared phase velocities. In the simplest case, the kernel is formulated based on the assumption that, at each frequency, a Rayleigh wave is propagating in a different homogeneous medium. A more accurate formulation, discussed in Haney and Tsai (2015), approximates the Rayleigh-wave eigenfunctions over a wide range of shear velocity profiles described by power laws. As pointed out in Haney and Tsai (2015), the relation in equation 27 is analogous to the Dix relation between squared layer velocities and squared stacking velocities in reflection seismology (Dix, 1955). Note the contrast in equation 27 and equation 16 or 19 — whereas equation 27 is based on an approximation; it is a direct relation between phase and shear velocity, not their perturbations. As a result, it can be used to define a good initial model for subsequent perturbational inversion.

We adopt a method for regularizing the linear-inversion problem based on weighted damped least squares. Data covariance and model covariance matrices, $\mathbf{C}_d$ and $\mathbf{C}_m$, are again chosen as in Gerstoft et al. (2006) and shown in equations 23 and 24. Note that because equation 27 is in terms of squared velocities, the data standard deviation σ_d has units of squared velocity. If a Rayleigh-wave velocity measurement is given by $\tilde{c}$ and its standard deviation is $\delta\tilde{c}$, then the standard deviation of $\tilde{c}^2$ is $2\tilde{c}\delta\tilde{c}$. As was the case for perturbational inversion, in the numerical codes, the model standard deviation is given as a user-supplied factor multiplied by the median of the data standard deviations. In fact, because two inversion parameters in equation 24, model standard deviation and correlation length, can be difficult to know a priori, we solve the linear-inversion problem over a range of the inversion parameters and average the acceptable models. The model standard deviation is given by a range of factors multiplied by the median of the data standard deviations. Similarly, the correlation length is given by a range of

factors multiplied by the median of the element thicknesses. Through testing, we have found a generic range for these factors: the model standard deviation factor runs from 1 to 20, and the correlation length factor runs from 10 to 1000. If no acceptable models are found over this range, based on the acceptable chi-squared window, the user is prompted to expand the range.

With the covariance matrices so chosen, the inversion proceeds by forming an augmented version of equation 27 (Snieder and Trampert, 1999; Aster et al., 2004):

$$\begin{bmatrix} \mathbf{C}_d^{-1/2}\mathbf{G} \\ \mathbf{C}_m^{-1/2} \end{bmatrix} \boldsymbol{\beta}^2 = \begin{bmatrix} \mathbf{C}_d^{-1/2}\mathbf{c}^2 \\ \mathbf{C}_m^{-1/2}\boldsymbol{\beta}_0^2 \end{bmatrix}, \tag{28}$$

where $\mathbf{c}^2$ is the squared phase-velocity data and $\boldsymbol{\beta}_0^2$ is the squared shear-wave velocity model obtained using the data-driven model-building method described by Xia et al. (1999). The method for obtaining $\boldsymbol{\beta}_0^2$ in Xia et al. (1999) is based on the simple mapping of a phase velocity measurement to a shear-wave velocity at the maximum sensitivity depth. The mapping in Xia et al. (1999) produces a model between the minimum and maximum sensitivity depths; to extend the model to the surface and to the base of the model, we apply linear extrapolation using robust estimates of the slope at the minimum and maximum sensitivity depths. The constraint containing $\boldsymbol{\beta}_0^2$ in equation 28 is designed to cause the inverted shear velocity model $\boldsymbol{\beta}^2$ to be close to the model obtained using the method of Xia et al. (1999) in areas with poor resolution, i.e., above and below the resolution depths associated with a band-limited dispersion curve. However, in areas with good resolution, the shear velocity model $\boldsymbol{\beta}^2$ generated by equation 28 will be an improvement over $\boldsymbol{\beta}_0^2$. We refer to this as a Dix-type inversion of surface waves (Haney and Tsai, 2015).

In the associated numerical codes, several features have been added to the Dix method originally described by Haney and Tsai (2015). Although Haney and Tsai (2015) formulate the Dix method for a single Poisson's ratio (0.25), the Dix method based on the homogeneous assumption can accommodate any Poisson's ratio in the codes. For a power-law assumption, the codes can implement the Dix method for a Poisson's ratio of 0.3 in addition to 0.25. Furthermore, the codes have extended the original Dix method, which only applied to phase velocities, to allow the inversion of group velocities. The extension to group velocities is discussed in Appendix F. A limitation of the Dix method is that it currently only applies to fundamental-mode phase or group velocity measurements. In addition, the method described in Haney and Tsai (2015) does not explicitly include a water layer. Future improvements to the Dix method will address these limitations.

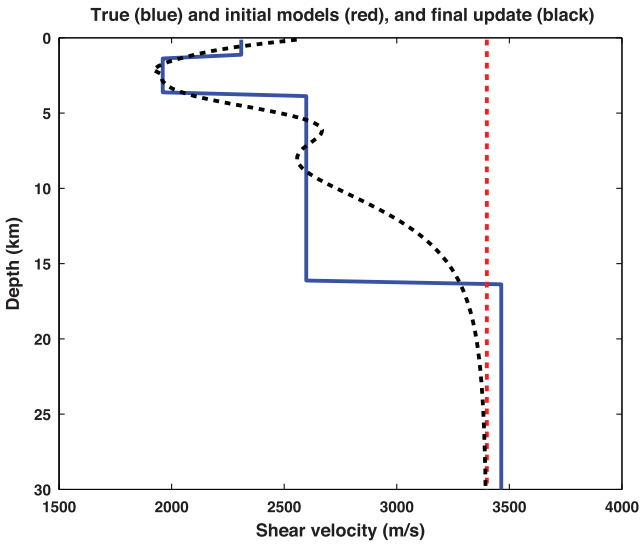

Figure 2. Shear velocity depth models for the crustal example: true model (blue solid), initial model (red dashed), and inverted model (black dashed).

SOFTWARE EXAMPLES

The entire collection of codes, called the RAYLEE package, consists of five MATLAB functions, 11 MATLAB scripts, and one text README file. Three phase velocity inversion examples are included in the package. One example performs inversion with a crustal-scale model using phase velocities measured for the fundamental and first higher mode between 0.1 and 0.65 Hz. Another example uses the same crustal-scale model, but with a 1 km thick water layer on top. The third inversion example uses noisy synthetic fundamental-mode data from the near-surface MODX model (Xia et al., 1999; Cercato, 2007), an initial model defined by Dix inversion, and an optimal non-uniform layering designed for Rayleigh waves. A final script shows results of some numerical tests for the Jacobian matrix produced by the finite-element method and for the computation of partial derivatives with respect to element thickness. Executing the codes associated with the three inversion examples reproduces Figures 2, 3, 4, 5, 6, 7, 8, 9, 10, and 11. The codes have been successfully run using MATLAB version R2014b on a laptop computer with 16 GB RAM, although the codes should be able to run with earlier versions of MATLAB and on machines with considerably less RAM. On the same machine, which has a clock speed of 2.3 GHz, each of the codes described below is able to execute in under 70 s. Although the descriptions below are not exhaustive, effort has been put into commenting the codes and so further detail regarding the MATLAB scripts and functions can be found in the source codes themselves.

The first example uses the crustal-scale model shown in Figure 2. The crustal-scale model contains a shallow low-velocity zone centered at approximately 3 km depth. Below the low-velocity zone, the shear-wave velocity increases to a value of 3.5 km/s, a normal value for the earth's crust. We generate synthetic data with 2.5% noise for the fundamental mode and first higher mode between 0.1 and 0.65 Hz (Figure 3), a typical frequency band for local scale ambient noise tomography (Brenguier et al., 2007). In this example, the fundamental mode and first higher mode will be jointly inverted. Luo et al. (2007) previously show that joint inversion of fundamental and higher modes produces deeper resolution than inversion of the fundamental mode alone. The inversion grid in this case is made up of uniform layers 250 m thick, and the initial model is taken to be a homogeneous half-space. To run the example, execute the following four MATLAB scripts:

```
≫ make_synthetic_ex1
≫ make_initial_model_ex1
≫ raylee_invert
≫ plot_results_ex1
```

As shown in Figure 3, data from the initial model in this case only include the fundamental mode because the initial model is homogeneous. The synthetic data contain first higher mode measure-

ments; however, the first higher mode does not exist over the entire frequency band from 0.1 to 0.65 Hz. The cutoff frequency for the first higher mode occurs between 0.1 and 0.2 Hz. In spite of these complexities, the perturbational inversion code is capable of progressively building a shear-wave velocity model that predicts higher mode dispersion in addition to the fundamental mode, as shown in Figure 3. The code does this by only including the fundamental-mode measurements in the first iteration and then including some of the higher mode measurements in the next iteration, when the depth model begins to support higher modes. The final update predicts 108 of the 109 phase velocity measurements. The lowest frequency phase velocity for the higher mode is not predicted because the initial model has a half-space velocity less than the true model. Thus, the modeled cutoff frequency is slightly less than the true cutoff frequency for the first higher mode.

The inversion reconstructs the true velocity model well down to a depth of approximately 10 km (Figure 2). Below that depth, resolution is lost and the inverted model reverts to the initial model. There is some loss of resolution at depths shallower than 1 km due to the band-limited measurements, but the inversion is capable of resolving the shallow low-velocity zone. The loss of shallow resolution can be seen from the inverted model being too fast at depths shallower than 1 km due to the initial model being too fast at those depths. Sensitivity kernels are presented in Figure 4, and they show that the fundamental mode has one lobe of sensitivity in depth, whereas the first higher mode has two lobes. The shallower sensitivity lobe of the first higher mode more or less coincides with the fundamental mode. The deeper lobe of sensitivity has the effect of extending the resolution in depth when the first higher mode is included in the inversion.

The second example uses the same model as the first example, with the exception that a 1 km thick water layer has been placed above the elastic medium. This simulates the situation of performing surface-wave inversion with ocean-bottom seismometers (Muyzert, 2007). Similar to the first example, the following four MATLAB scripts execute the code:

```
≫ make_synthetic_ex2
≫ make_initial_model_ex2
≫ raylee_invert
≫ plot_results_ex2
```

Figures 5–7 show similar plots of the depth models, phase-velocity data, and sensitivity kernels as for the first example. A homogeneous initial model has been used again, as shown in Figure 5, and the true model has been adequately resolved to a depth of approximately 8 km — slightly shallower with respect to the water-solid interface than the depth of resolution when a water layer was not included. This means that the presence of a water layer causes the guided Scholte waves to be slower at the same frequency compared with the Rayleigh waves in the first example, as shown by comparing

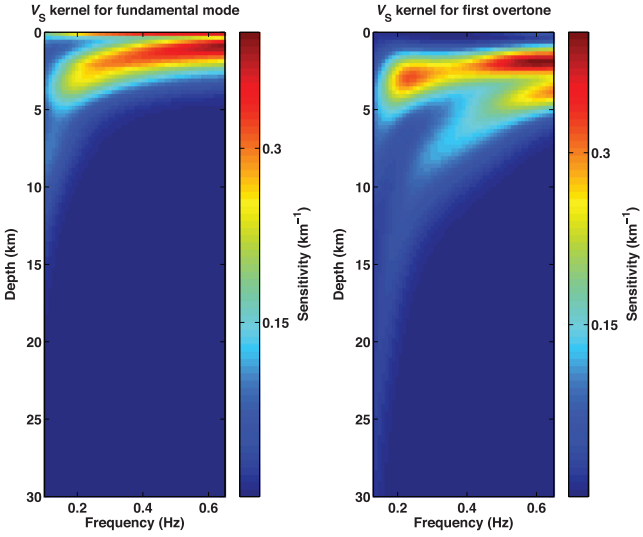

Figure 4. Fundamental mode and first overtone sensitivity kernels of the final inversion update for the crustal example.

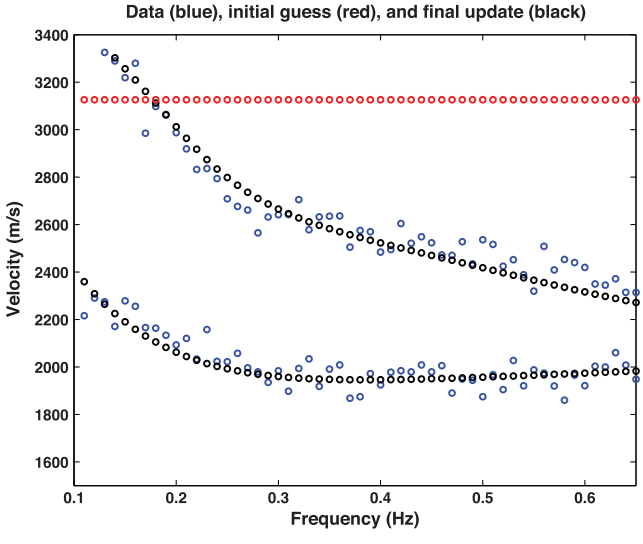

Figure 3. Phase velocity dispersion curves for the crustal example: noisy synthetic fundamental mode and first overtone data (blue), fundamental-mode data from initial model (red), and predicted fundamental mode and first overtone data from inversion result (black).

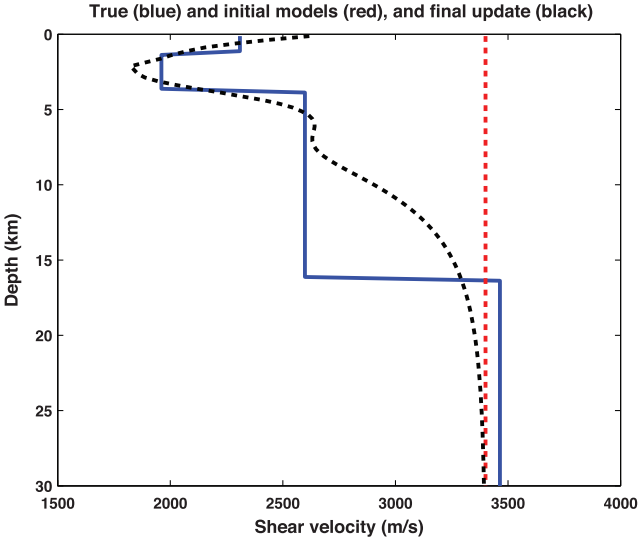

Figure 5. Shear velocity depth models for the crustal example with a water layer on top: true model (blue solid), initial model (red dashed), and inverted model (black dashed). Depth refers to the vertical distance below the water-solid interface, and the water layer is not shown.

Figures 3 and 6. The slower phase velocity translates into a shorter wavelength and, therefore, a shallower maximum depth of sensitivity.

Synthetic data from the initial model in Figure 6 are dispersive and contain some higher mode measurements, in contrast to the first example. This is due to the presence of the water layer on the top of the homogeneous solid earth portion of the initial model. Although some higher mode measurements exist in the synthetic data from the initial model, the inversion is able to progressively include more of the higher modes in subsequent iterations and finally fit 108 of the 109 phase velocity measurements, as before. In spite of the solid earth portion of the model being identical to the first example, the sensitivity kernels for the model with a water layer shown in Figure 7 are significantly different from Figure 4. A greater similarity between the kernels exists at lower frequencies, but at frequencies greater than 0.4 Hz, the presence of the water layer changes the kernels and transfers a majority of the sensitivity in the first higher mode to depths shallower than 5 km.

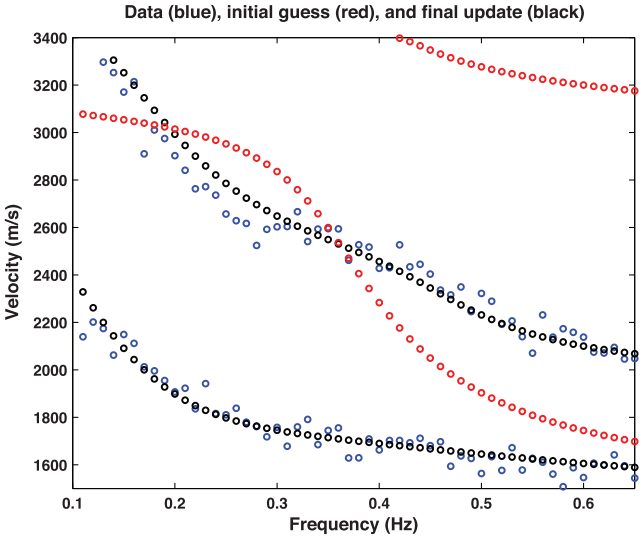

Figure 6. Phase velocity dispersion curves for the crustal example with a water layer on top: noisy synthetic fundamental mode and first overtone data (blue), fundamental mode, and first overtone data from initial model (red), and predicted fundamental mode and first overtone data from inversion result (black).

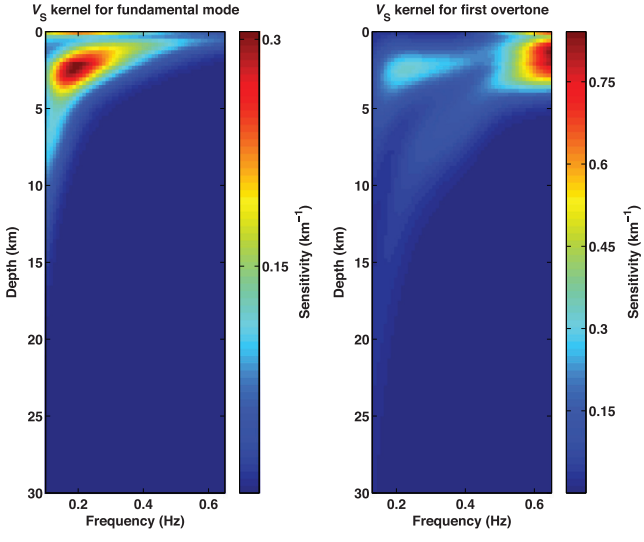

Figure 7. Fundamental mode and first overtone sensitivity kernels of the final-inversion update for the crustal example with a water layer on top.

The final inversion example uses the near-surface MODX model (Xia et al., 1999; Cercato, 2007) instead of a crustal-scale model. This example also uses a Dix-type inversion to define an accurate initial model and makes use of an optimal inversion grid of layers, as discussed in Appendix E. To run the example, the following four MATLAB scripts execute the code:

≫ make_synthetic_modx
≫ make_initial_model_dix
≫ raylee_invert
≫ plot_results_modx

Figure 8 shows the chi-squared misfit for the Dix-inversion step that produces the initial model, and Figures 9–11 show the models, data, and sensitivity kernel, respectively, from the perturbational inversion. The synthetic MODX data have been produced with 2% noise added and the inversions, nonperturbational and perturbational, have used an optimal nonuniform layering. As stated earlier, the Dix inversion scans over a range of model standard deviation factors and correlation-length factors to find an ensemble of models that fit the data between the minimum and maximum chi-squared values within the approximation of Dix-type Rayleigh-wave modeling. The chi-squared values for these models are shown between the dashed white lines in Figure 8. The shear-wave velocities of those models are averaged to yield the final Dix model. Note that the Dix inversion was performed with the homogeneous formulation (Haney and Tsai, 2015) and a Poisson's ratio of 0.45. The depth profile output by the Dix step, shown as the dashed red line in Figure 9,

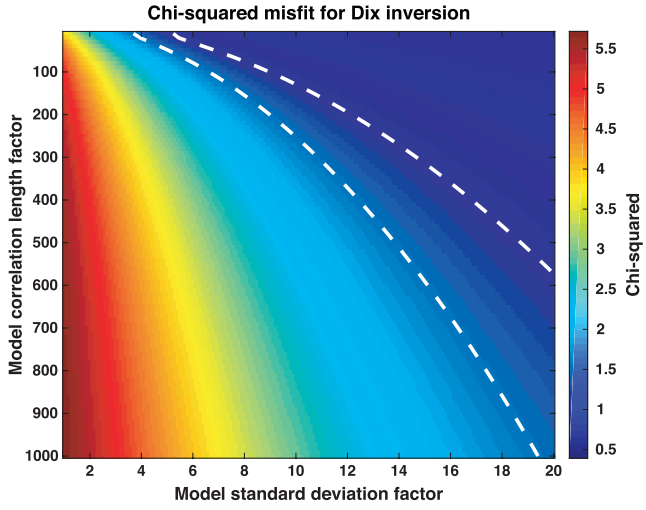

Figure 8. Chi-squared misfit for Dix-type phase inversion of noisy synthetic data from the MODX model plotted over a range of smoothing lengths and model standard deviations. The dashed white lines show the acceptable bounds on chi-squared from 1 to 1.5 for models to be considered. The initial model for the subsequent perturbational phase inversion is obtained by taking the average of the acceptable models.

is then used as an initial model for perturbational inversion, which converges to a final model in six iterative steps. During the perturbational inversion, the Poisson's ratio is held constant at 0.45. The final model is observed to match reasonably well a smoothed version of the true model, and the data fit has been improved during the perturbational step, as shown in Figure 10. Although the model was improved, the Dix step was successful in defining an initial model that was close enough to the true model to allow convergence.

The sensitivity kernel for the final update of the perturbational inversion is shown in Figure 11, and it displays complex behavior near 15 Hz, with sensitivity concentrated in the uppermost portion of the model. We note that the first two software examples with the crustal-scale model could have also used the Dix step to define a better initial model than the homogeneous one. We took a homogeneous initial model in those cases to illustrate how the codes treated higher-mode surface waves, but in practice, it would be better to use the Dix inversion step to develop a more precise initial model prior to the perturbational inversion. Beyond the advantage of faster modeling with the nonuniform grid, there is also the advantage for inversion of having fewer model parameters and a smaller possibility of numerical instability.

The final software example outputs the results of a numerical test to the MATLAB command line. The test can be run with the following script:

```
≫ numerical_tests
```

The script outputs a Jacobian matrix for a crustal model and three vectors containing partial derivatives with respect to layer thickness. The Jacobian matrix is computed by the codes in this paper and can be directly compared with the Jacobian matrices for a variety of Rayleigh-wave codes in Cercato (2007). This comparison shows the codes in this paper are capable of calculating the Jacobian matrix to a high degree of accuracy. The three vectors output by this script show partial derivatives with respect to thickness of the crustal layer in the MODN crustal model discussed in Cercato (2007). These partial derivatives are computed in three ways: (1) using a variational method, (2) a brute-force method by thinning the crustal layer slightly, and (3) a brute-force method by thickening the crustal layer slightly. The variational method is preferred and is provided in the codes, but the brute-force methods show that the variational approach is capable of computing these layer thickness partial derivatives. Such partial derivatives with respect to layer thickness, in contrast to the more well-known partial derivatives with respect to material properties, can be useful for surface-wave inversions in which interfaces are explicitly included in the model (e.g., inversions for the Moho).

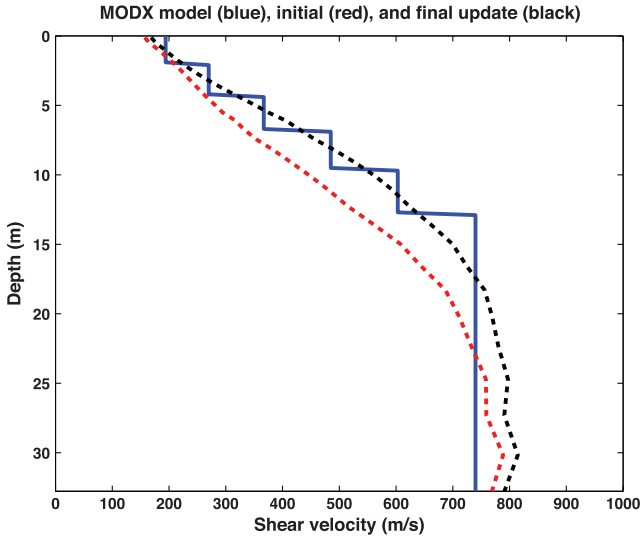

Figure 9. Shear velocity depth models for the MODX example using phase velocities: true model (blue solid), initial model (red dashed), and inverted model (black dashed). The initial model is generated using a Dix-type phase inversion for Rayleigh waves.

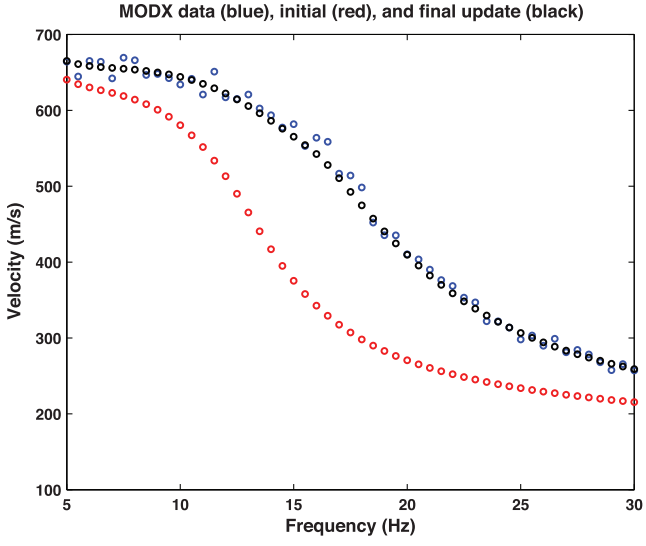

Figure 10. Phase velocity dispersion curves for the MODX example: noisy synthetic data (blue), data from the initial model (red), and predicted data from the inversion result (black). The initial model is generated using a Dix-type phase inversion for Rayleigh waves.

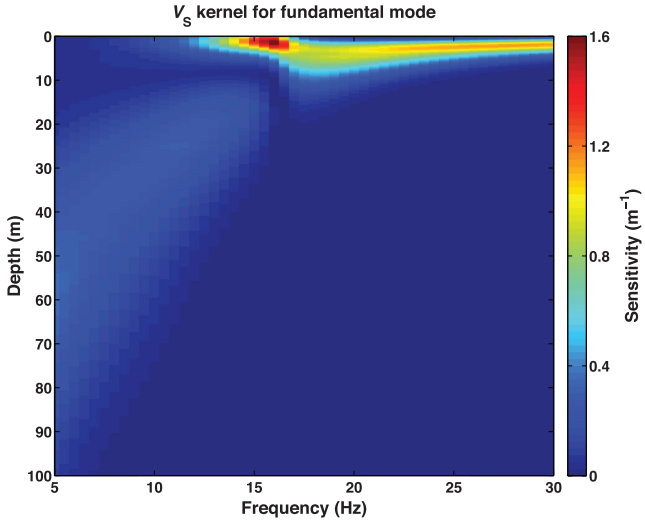

Figure 11. Fundamental mode phase-sensitivity kernel of the final-inversion update for the MODX example.

CONCLUSION

The modeling of Rayleigh-wave phase velocity, group velocity, and mode shapes can be performed with eigenvalue/eigenvector methods without recourse to root finding. Although the method may not be as fast as the most efficient techniques based on root finding, the method is simple and reasonably fast. We have presented a set of perturbational inversion codes that can invert arbitrary collections of phase/group velocity measurements of any mode. An accurate initial model can be generated using the recently introduced Dix-type nonperturbational inversion. Additional properties of the codes include the ability to add a water layer on the top of an elastic model and the automatic generation of a nonuniform layering optimally designed for the sensitivity of Rayleigh waves. Numerical tests show that the method is capable of producing a Jacobian matrix in agreement with previously published studies and also of computing partial derivatives with respect to layer thickness. We have also provided three examples of performing inversions with the codes using synthetic data generated for crustal-scale and near-surface models.

ACKNOWLEDGMENTS

Comments by P. Dawson (USGS), E. Muyzert, and an anonymous reviewer have helped to improve this manuscript. Any use of trade, firm, or product names is for descriptive purposes only and does not imply endorsement by the U.S. government.

APPENDIX A

ELEMENTAL MATRICES

Matrices $\mathbf{B}_2$, $\mathbf{B}_1$, $\mathbf{B}_0$, and $\mathbf{M}$ are discussed in Kausel (2005), but we describe them briefly here for completeness. These matrices are best understood as being assembled from fundamental 4×4 matrices known as elemental matrices. For instance, Kausel (2005) shows that the elemental mass matrix associated with the Kth element, $\tilde{\mathbf{M}}_K$, is

$$\tilde{\mathbf{M}}_K = h_K \begin{bmatrix} \rho_K/3 & 0 & \rho_K/6 & 0 \\ 0 & \rho_K/3 & 0 & \rho_K/6 \\ \rho_K/6 & 0 & \rho_K/3 & 0 \\ 0 & \rho_K/6 & 0 & \rho_K/3 \end{bmatrix}. \tag{A-1}$$

The process known as "mass lumping" replaces this matrix by a diagonal matrix, whose entries are equal to the row sum:

$$\tilde{\mathbf{M}}_K^L = h_K \begin{bmatrix} \rho_K/2 & 0 & 0 & 0 \\ 0 & \rho_K/2 & 0 & 0 \\ 0 & 0 & \rho_K/2 & 0 \\ 0 & 0 & 0 & \rho_K/2 \end{bmatrix}. \tag{A-2}$$

The full-mass matrix $\mathbf{M}$ can be assembled from this 4×4 matrix by adding individual 4×4 matrices in the recursive manner shown in Figure 4 of Lysmer (1970). A similar procedure applies for the stiffness matrices $\mathbf{B}_0$, $\mathbf{B}_1$, and $\mathbf{B}_2$, although the 4×4 matrices in these cases are not lumped prior to assembly as in the case of the mass matrix $\mathbf{M}$.

APPENDIX B

GROUP VELOCITY

As shown by Lysmer (1970), the group velocity at a single frequency can be obtained without numerical differentiation of the phase velocity dispersion curve once the phase velocity and eigenfunction are known. This result is given here for completeness, but also because it provides an introduction to perturbational techniques developed further in Appendix E for the inverse problem.

From equation 3, the generalized quadratic eigenvalue problem for Rayleigh waves can be written as

$$(\mathbf{B}_k - \omega^2 \mathbf{M})\mathbf{v} = 0, \tag{B-1}$$

where $\mathbf{B}_k = k^2\mathbf{B}_2 + k\mathbf{B}_1 + \mathbf{B}_0$. To find an expression for group velocity, we perturb the wavenumber k and frequency ω while keeping the material properties constant. This leads to the following perturbed equation:

$$\left(\mathbf{B}_k + \frac{\partial \mathbf{B}_k}{\partial k}\delta k - (\omega + \delta\omega)^2 \mathbf{M}\right)(\mathbf{v} + \boldsymbol{\delta}\mathbf{v}) = 0. \tag{B-2}$$

Given the equality in equation B-1, this perturbed equation gives to first order

$$(\mathbf{B}_k - \omega^2 \mathbf{M})\boldsymbol{\delta}\mathbf{v} + \frac{\partial \mathbf{B}_k}{\partial k}\delta k \mathbf{v} - 2\omega\delta\omega\mathbf{M}\mathbf{v} = 0. \tag{B-3}$$

We now multiply equation B-3 from the left by $\mathbf{v}^T$. The first term on the left side of equation B-3 vanishes due to equation B-1 because $\mathbf{B}_k$ and $\mathbf{M}$ are symmetric matrices, yielding

$$2\omega\delta\omega\mathbf{v}^T\mathbf{M}\mathbf{v} = \mathbf{v}^T \frac{\partial \mathbf{B}_k}{\partial k}\delta k \mathbf{v}. \tag{B-4}$$

Given that $\partial \mathbf{B}_k/\partial k = 2k\mathbf{B}_2 + \mathbf{B}_1$, an expression for the group velocity U is

$$U = \frac{\delta\omega}{\delta k} = \frac{\mathbf{v}^T(2k\mathbf{B}_2 + \mathbf{B}_1)\mathbf{v}}{2\omega\mathbf{v}^T\mathbf{M}\mathbf{v}}. \tag{B-5}$$

APPENDIX C

FORWARD MODELING WITH A WATER LAYER

Guided waves of P-SV type are excited when a water or fluid layer overlies an elastic medium. The guided waves in this case are called either Stoneley or Scholte waves, depending on whether the phase velocity of the guided waves is less than (Stoneley) or greater than (Scholte) the propagation velocity in the fluid. For example, if the water layer were homogeneous with a propagation velocity of 1500 m/s and the guided wave had a phase velocity less than 1500 m/s, then it would be called a Stoneley wave because it would be exponentially trapped above and below the fluid-solid interface. If the guided wave instead had a phase velocity greater than 1500 m/s, it would only be exponentially trapped in the direction of the solid earth. For these reasons, nondispersive Stoneley waves exist for a model of a fluid half-space over an elastic half-space (Strick and Ginzbarg, 1956). Scholte waves, on the other hand, only

exist for a water layer of finite depth because, in that case, the presence of the water surface acts to effectively trap the guided wave from above.

Komatitsch et al. (2000) demonstrate how to include a fluid-solid interface in a grid-based method in the weak formulation. Although Komatitsch et al. (2000) specifically work with a spectral-element method, the same concepts apply to finite-element methods. Haney (2009) uses the finite-element method to model guided waves in a fluid by considering sound waves in the atmosphere. In fact, fluid finite elements have a similar form to finite elements in electromagnetics, which were used by Haney et al. (2010) to model guided waves in ground-penetrating radar data. Here, we combine fluid finite elements with solid finite elements to model a water layer on the top of an elastic medium. In the fluid, pressure is computed at each node, whereas the particle velocity is computed at each node in the solid. By organizing the N unknown nodal displacements with the pressure eigenfunction in the fluid (p) and alternating horizontal eigenfunction (r_1) and vertical eigenfunction (r_2) components in the solid, we obtain

$$\mathbf{v} = [\ \ldots \quad p^{Nf-1} \quad p^{Nf} \quad r_1^{Nf+1} \quad r_2^{Nf+1} \quad r_1^{Nf+2} \quad r_2^{Nf+2} \quad \ldots\ ]^T, \tag{C-1}$$

where Nf is the number of finite elements in the fluid layer. With this organization of the nodal displacements, the complete Stoneley- or Scholte-wave eigenvector is given by a generalized quadratic eigenvalue problem in terms of the wavenumber k:

$$(k^2\mathbf{B}_2 + k\mathbf{B}_1 + \mathbf{B}_0)\mathbf{v} = \omega^2\mathbf{M}\mathbf{v} - \omega\mathbf{C}\mathbf{v}, \tag{C-2}$$

where the form is the same as equation 3, except that a coupling matrix $\mathbf{C}$ appears on the right side (Komatitsch et al., 2000). The symmetric coupling matrix is extremely sparse and only has two nonzero entries in the Nf and $(Nf+2)$ rows. Because the coupling matrix $\mathbf{C}$ does not depend on material properties, the inclusion of a known water layer does not affect the form of the perturbational inversion formula developed for Rayleigh waves (equation 9). Moreover, in the inversion codes, only the material properties in the solid are altered — the depth, acoustic-wave speed, and density of the water layer are assumed to be known. The presence of the coupling matrix does, however, change the expression for the group velocity shown in Appendix B. When a water layer exists, group velocity is instead given by

$$U = \frac{\delta\omega}{\delta k} = \frac{\mathbf{v}^T(2k\mathbf{B}_2 + \mathbf{B}_1)\mathbf{v}}{2\omega\mathbf{v}^T\mathbf{M}\mathbf{v} - \mathbf{v}^T\mathbf{C}\mathbf{v}}. \tag{C-3}$$

The final consideration for a water layer concerns the upper bound on the wavenumber eigenvalue. As discussed in the main text, when no water layer is present, the upper bound is found by computing the half-space Rayleigh-wave velocity given the material properties at each node in the finite-element model and then taking the minimum. When a water layer is present, this procedure is modified by computing the nondispersive Stoneley-wave velocity at each node in the finite-element model and then taking the minimum. For this reason, a MATLAB function is included in the codes, which computes Stoneley-wave velocity for a given fluid half-space overlying a solid half-space. The Stoneley-wave velocity in this case is the solution of an eighth-order polynomial (Strick and Ginzbarg, 1956).

APPENDIX D

OPTIMAL LAYERS FOR RAYLEIGH WAVES

The grid-based approaches described in this paper require a user-prescribed layering. The simplest layering is a stack of layers with equal thickness; however, such a layering would not be most efficient because properly sampling the Rayleigh waves at shallow depths would oversample the waves deeper in the model. Oversampling translates into unnecessarily longer execution times for the code, and inversion with an oversampled grid can lead to instabilities. Here, we explore the possibility of defining an optimal layering for Rayleigh-wave modeling based on a phase velocity dispersion curve. A similar approach has been used by Ma and Clayton (2016) to obtain a layering for surface wave inversion.

We begin with the approximate maximum sensitivity depth of Rayleigh waves, which is taken to be proportional to wavelength ℓ:

$$z = a\ell, \tag{D-1}$$

where a is a factor equal to 0.63 (Xia et al., 1999) or 0.5 (Haney and Tsai, 2015). Given a phase-velocity dispersion curve, we can find the minimum and maximum wavelengths, $\ell_{\min}$ and $\ell_{\max}$, and in turn the minimum and maximum depths:

$$z_{\min} = a\ell_{\min}, \tag{D-2}$$

$$z_{\max} = a\ell_{\max}. \tag{D-3}$$

We seek to find a particular layering for Rayleigh waves that follows from these relations. First, we focus on the depth interval from $z_{\min}$ to $z_{\max}$ and discuss the intervals $(0, z_{\min})$ and $(z_{\max}, \infty)$ later. We assume that there is a desired density of layers per wavelength

$$r(\ell) = n/\ell, \tag{D-4}$$

where n is the number of layers to be sampled within a single wavelength. Setting this quantity is based on sampling considerations similar to time-domain wave-propagation algorithms (Marfurt, 1984). Given the relation between depth and wavelength in equation D-1, we can express the layer density in terms of the depth

$$r(z) = na/z. \tag{D-5}$$

Integration of the layer density from $z_{\min}$ to a certain depth yields the cumulative number of layers at that depth

$$\int_{z_{\min}}^{z} r(z')dz' = N(z). \tag{D-6}$$

Performing the integration with the expression for r given in equation D-5 gives

$$N(z) = na\ \ln\left(\frac{z}{z_{\min}}\right). \tag{D-7}$$

Note that $N(z_{\min}) = 0$; thus, N does not include any layers between $(0, z_{\min})$ that we have not addressed yet. From equation D-7, we can estimate the maximum number of layers, $N_{\max}$

$$N_{\max} = N(z_{\max}) = na\,\ln\left(\frac{z_{\max}}{z_{\min}}\right). \tag{D-8}$$

For $N_{\max}$ to be an integer, we round $N_{\max}$ up and denote this value as $\tilde{N}_{\max}$. Rounding up means that the deepest layer between $z_{\min}$ and $z_{\max}$ will be slightly thinner than it should be. To find the layers, we rewrite equation D-7 in terms of the depths of the layer interfaces

$$z(N) = z_{\min}\,\exp(N/na). \tag{D-9}$$

Because there are $\tilde{N}_{\max}$ layers, there are $\tilde{N}_{\max}+1$ interfaces and the interface index runs from zero to $\tilde{N}_{\max}$. The deepest interface is at $z_{\max}$, and the thickness of a layer is given by the difference in the neighboring interfaces. For example, the shallowest layer has a thickness equal to $z(1)-z(0)$. To get an idea of the behavior of the layer thicknesses, we can approximate the finite differencing of the layer interfaces by taking the derivative of equation D-9 with respect to N. The derivative is given by

$$\frac{\partial z}{\partial N} = \frac{z_{\min}}{na}\exp(N/na). \tag{D-10}$$

This expression is approximately equal to the thickness of the Nth layer and shows that the thicknesses increase more or less exponentially as a function of the layer number. This represents an optimal layering based on the sensitivity of Rayleigh waves.

The layering in the intervals $(0, z_{\min})$ and $(z_{\max}, \infty)$ still needs to be addressed. According to the relation in equation D-1, Rayleigh waves are not sensitive to these depths; however, equation D-1 is approximate and some sensitivity exists in these depth ranges (Haney and Tsai, 2015). A conservative approach to layering in the intervals $(0, z_{\min})$ and $(z_{\max}, \infty)$ is to decrease $z_{\min}$ and increase $z_{\max}$ from their theoretical values in equations D-2 and D-3. Once those values have been adjusted to values given by $\tilde{z}_{\min}$ and $\tilde{z}_{\max}$, the remaining interval $(0, \tilde{z}_{\min})$ can be covered by layers of uniform thickness given by the minimum layer thickness between $\tilde{z}_{\min}$ and $\tilde{z}_{\max}$. If the length of the interval $(0, \tilde{z}_{\min})$ is not a multiple of the minimum layer thickness, the remaining portion is accommodated at the top of the model by an even thinner layer. The interval $(\tilde{z}_{\max}, \infty)$ can be treated as single layer. Note that, with this distribution, layer thicknesses do not decrease with depth at any point in the model.

APPENDIX E

PERTURBATION THEORY

In Appendix B, we perturbed wavenumber and frequency while keeping the material properties the same to obtain an expression for the group velocity. Here, we perturb the wavenumber and material properties and fix the frequency. This approach leads to a first-order result relating perturbations in phase velocity to perturbations in the material properties. Such a formula forms the basis for perturbational inversion of Rayleigh-wave dispersion curves.

The perturbation of the material properties and wavenumber in equation 3 is expressed as

$$\begin{aligned}
&\left((k+\delta k)^2\left[\mathbf{B}_2 + \sum_{i=1}^{N}\frac{\partial \mathbf{B}_2}{\partial \mu_i}\delta\mu_i + \sum_{i=1}^{N}\frac{\partial \mathbf{B}_2}{\partial \lambda_i}\delta\lambda_i\right]\right.\\
&+ (k+\delta k)\left[\mathbf{B}_1 + \sum_{i=1}^{N}\frac{\partial \mathbf{B}_1}{\partial \mu_i}\delta\mu_i + \sum_{i=1}^{N}\frac{\partial \mathbf{B}_1}{\partial \lambda_i}\delta\lambda_i\right]\\
&\left.+ \left[\mathbf{B}_0 + \sum_{i=1}^{N}\frac{\partial \mathbf{B}_0}{\partial \mu_i}\delta\mu_i + \sum_{i=1}^{N}\frac{\partial \mathbf{B}_0}{\partial \lambda_i}\delta\lambda_i\right]\right)(\mathbf{v}+\boldsymbol{\delta}\mathbf{v})\\
&= \omega^2\left[\mathbf{M} + \sum_{i=1}^{N}\frac{\partial \mathbf{M}}{\partial \rho_i}\delta\rho_i\right](\mathbf{v}+\boldsymbol{\delta}\mathbf{v}).
\end{aligned} \tag{E-1}$$

Because $\mathbf{B}_2$, $\mathbf{B}_1$, $\mathbf{B}_0$, and $\mathbf{M}$ are symmetric, the following identity is valid:

$$\mathbf{v}^T(k^2\mathbf{B}_2 + k\mathbf{B}_1 + \mathbf{B}_0)\boldsymbol{\delta}\mathbf{v} = \mathbf{v}^T\omega^2\mathbf{M}\boldsymbol{\delta}\mathbf{v}. \tag{E-2}$$

Substituting this relation together with equation 3 into equation E-1 and left multiplying by $\mathbf{v}^T$ gives, to first order

$$\begin{aligned}
\delta k\mathbf{v}^T[2k\mathbf{B}_2+\mathbf{B}_1]\mathbf{v} = {}& \omega^2\mathbf{v}^T\left[\sum_{i=1}^{N}\frac{\partial \mathbf{M}}{\partial \rho_i}\delta\rho_i\right]\mathbf{v}\\
&-\mathbf{v}^T\left[\sum_{i=1}^{N}\frac{\partial(k^2\mathbf{B}_2+k\mathbf{B}_1+\mathbf{B}_0)}{\partial \mu_i}\delta\mu_i\right]\mathbf{v}\\
&-\mathbf{v}^T\left[\sum_{i=1}^{N}\frac{\partial(k^2\mathbf{B}_2+k\mathbf{B}_1+\mathbf{B}_0)}{\partial \lambda_i}\delta\lambda_i\right]\mathbf{v}.
\end{aligned} \tag{E-3}$$

Using the expression for group velocity in equation 6 and the fact that $\delta k/k = -\delta c/c$, this first-order result leads to equation 9.

APPENDIX F

DIX MODELING OF PHASE AND GROUP VELOCITIES

The Dix approximation for surface waves (Haney and Tsai, 2015) can be expressed in the continuous limit as

$$c^2(k) = \int_0^{\infty}\frac{\partial f(k,z)}{\partial z}\beta^2(z)dz, \tag{F-1}$$

in which c is the phase velocity, k is the wavenumber ($k=\omega/c$ where ω is the angular frequency), z is the depth, β is the shear-wave velocity, and $\partial f(k,z)/\partial z$ is the kernel function relating c^2 to β^2. Equation F-1 shows that c^2 and β^2 can be considered as dual variables related through an integral transform between k and z. The specific form of the kernel function (Haney and Tsai, 2015) shows that the integral transform in equation F-1 is similar to a Laplace transform.

Equation F-1 can be used to forward model a phase-dispersion curve given a shear velocity depth profile, within the approximation of the Dix-type relation. The forward modeling is performed by first scanning over wavenumber k and mapping out phase velocity c as a function of wavenumber, $c(k)$. Once $c(k)$ has been mapped out, phase velocity as a function of frequency can be obtained by interpolating $c(k)$ onto a raster of frequencies ω, thereby producing

$c(\omega)$. For a Poisson's ratio of 0.25, the scan over k can proceed from $k_{\min} = \omega_{\min}/(0.9194\beta_{\max})$ to $k_{\max} = \omega_{\max}/(0.9194\beta_{\min})$ and cover all frequencies of interest.

We now consider the possibility of forward modeling group velocity curves within the Dix approximation based on a homogeneous assumption (Haney and Tsai, 2015). For this, we write the group velocity U as a function of the wavenumber k as follows:

$$U(k) = \frac{\partial\omega}{\partial k} = \frac{\partial[kc(k)]}{\partial k} = c(k) + k\frac{\partial c(k)}{\partial k} = c(k) + \frac{k}{2c(k)}\frac{\partial c^2(k)}{\partial k}. \quad \text{(F-2)}$$

The hallmark of the Dix approximation is the proportionality of squared observable velocities (e.g., stacking or phase velocities) to squared layer velocities (e.g., shear velocities for the surface-wave Dix-type relation). To see if such a relation holds for group velocities, we square equation F-2 to obtain

$$U^2(k) = c^2(k) + k\frac{\partial c^2(k)}{\partial k} + \frac{k^2}{4c^2(k)}\left(\frac{\partial c^2(k)}{\partial k}\right)^2. \quad \text{(F-3)}$$

We now make the approximation that the amount of dispersion is relatively small, i.e.

$$\frac{k}{c^2(k)}\frac{\partial c^2(k)}{\partial k} \ll 1, \quad \text{(F-4)}$$

so that the third term on the right side of equation F-3 can be neglected. The approximation of a small amount of dispersion is consistent with the applicability of the Dix-type relation based on a homogeneous assumption to weakly heterogeneous layered structures. The second term on the right side of equation F-3 therefore represents the lowest order correction to phase velocity to obtain group velocity. Taking the first two terms on the right side of equation F-3, we find the following expression for group velocity:

$$U^2(k) = \int_0^\infty \frac{\partial}{\partial z}\left[f(k,z) + k\frac{\partial f(k,z)}{\partial k}\right]\beta^2(z)dz. \quad \text{(F-5)}$$

This equation has the same form as equation F-1, but with a different kernel function. Thus, equation F-5 represents a Dix-type relation for group velocity.

The final issue for modeling group velocity curves is that equation F-5 provides a means for mapping out group velocity U as a function of wavenumber $U(k)$. However, in practice, we measure the group velocity as a function of frequency $U(\omega)$. Strictly speaking, phase velocities are needed to convert $U(k)$ to $U(\omega)$. If only group velocities are available, then we must make an additional approximation within the interpolation step to relate k and ω. The simplest approach would be to approximate frequency as $\omega \approx kU$. Although simple, this approach is again consistent with the weak heterogeneity and small dispersion approximation inherent in the Dix-type relation based on a homogeneous assumption.

For the Dix-type relation based on power-law velocity profiles, we retain all three terms in equation F-3 because dispersion is not assumed to be small. In this case, we find a straightforward relation between group and phase velocity for a power-law shear velocity profile with exponent α given by

$$U = (1-\alpha)c. \quad \text{(F-6)}$$

This relation between group and phase velocity for power-law shear velocity profiles has been noted before by Tsai et al. (2012) and Tsai and Atiganyanun (2014). It holds in this case because the Dix-type relation has the same frequency scaling as the exact solution in power-law shear velocity profiles (Haney and Tsai, 2015). Therefore, the Dix-type relation for group velocity follows from the phase velocity together with a nominal value for the power-law exponent α.

REFERENCES

Aki, K., and P. G. Richards, 1980, Quantitative seismology: W. H. Freeman and Company.

Aster, R., B. Borchers, and C. Thurber, 2004, Parameter estimation and inverse problems: Elsevier Academic Press.

Brenguier, F., N. M. Shapiro, M. Campillo, A. Nercessian, and V. Ferrazzini, 2007, 3-D surface wave tomography of the Piton de la Fournaise volcano using seismic noise correlations: Geophysical Research Letters, **34**, L02305, doi: 10.1029/2006GL028586.

Cercato, M., 2007, Computation of partial derivatives of Rayleigh-wave phase velocity using second-order subdeterminants: Geophysical Journal International, **170**, 217–238, doi: 10.1111/j.1365-246X.2007.03383.x.

Cercato, M., 2008, Addressing non-uniqueness in linearized multichannel surface wave inversion: Geophysical Prospecting, **57**, 27–47, doi: 10.1111/j.1365-2478.2007.00719.x.

Chouet, B., G. De Luca, G. Milana, P. Dawson, M. Martini, and R. Scarpa, 1998, Shallow velocity structure of stromboli volcano, Italy, derived from small-aperture array measurements of strombolian tremor: Bulletin of the Seismological Society of America, **88**, 653–666.

Dix, C. H., 1955, Seismic velocities from surface measurements: Geophysics, **20**, 68–86, doi: 10.1190/1.1438126.

Dorman, J., and M. Ewing, 1962, Numerical inversion of seismic surface wave dispersion data and crust-mantle structure in the New York-Pennsylvannia area: Journal of Geophysical Research, **67**, 5227–5241, doi: 10.1029/JZ067i013p05227.

Garofalo, F., S. Foti, F. Hollender, P. Y. Bard, C. Cornou, B. R. Cox, M. Ohrnberger, D. Sicilia, M. Asten, G. Di Giulio, T. Forbriger, B. Guillier, K. Hayashi, A. Martin, S. Matsushima, D. Mercerat, V. Poggi, and H. Yamanaka, 2016, InterPACIFIC project: Comparison of invasive and non-invasive methods for seismic site characterization. Part I: Intra-comparison of surface wave methods: Soil Dynamics and Earthquake Engineering, **82**, 222–240, doi: 10.1016/j.soildyn.2015.12.010.

Gerstoft, P., K. G. Sabra, P. Roux, W. A. Kuperman, and M. C. Fehler, 2006, Green's functions extraction and surface-wave tomography from microseisms in southern California: Geophysics, **71**, no. 4, SI23–SI31, doi: 10.1190/1.2210607.

Gouveia, W. P., and J. A. Scales, 1998, Bayesian seismic waveform inversion parameter estimation and uncertainty analysis: Journal of Geophysical Research, **103**, 2759–2779, doi: 10.1029/97JB02933.

Haney, M. M., 2009, Infrasonic ambient noise interferometry from correlations of microbaroms: Geophysical Research Letters, **36**, L19808, doi: 10.1029/2009GL040179.

Haney, M. M., K. T. Decker, and J. H. Bradford, 2010, Permittivity structure derived from group velocities of guided GPR pulses, *in* R. D. Miller, J. H. Bradford, and K. Holliger, eds., Advances in near surface seismology and ground penetrating radar: SEG, 167–184.

Haney, M. M., and V. C. Tsai, 2015, Nonperturbational surface-wave inversion: A Dix-type relation for surface waves: Geophysics, **80**, no. 6, EN167–EN177, doi: 10.1190/geo2014-0612.1.

Karpfinger, F., H.-P. Valero, B. Gurevich, A. Bakulin, and B. Sinha, 2010, Spectral-method algorithm for modeling dispersion of acoustic modes in elastic cylindrical structures: Geophysics, **75**, no. 3, H19–H27, doi: 10.1190/1.3380590.

Kausel, E., 2005, Wave propagation modes from simple systems to layered soils, *in* C. G. Lai, and K. Wilmanski, eds., Surface waves in geomechanics: Direct and inverse modeling for soil and rocks: Springer-Verlag, 165–202.

Komatitsch, D., C. Barnes, and J. Tromp, 2000, Wave propagation near a fluid-solid interface: A spectral-element approach: Geophysics, **65**, 623–631, doi: 10.1190/1.1444758.

Lehoucq, R. B., D. C. Sorensen, and C. Yang, 1998, ARPACK users' guide: Solution of large scale eigenvalue problems with implicitly restarted Arnoldi methods: SIAM.

Luo, Y., J. Xia, J. Liu, Q. Liu, and S. Xu, 2007, Joint inversion of high-frequency surface waves with fundamental and higher modes: Journal of Applied Geophysics, **62**, 375–384, doi: 10.1016/j.jappgeo.2007.02.004.

Lysmer, J., 1970, Lumped mass method for Rayleigh waves: Bulletin of the Seismological Society of America, **60**, 89–104.

Ma, Y., and R. Clayton, 2016, Structure of the Los Angeles Basin from ambient noise and receiver functions: Geophysical Journal International, **206**, 1645–1651, doi: 10.1093/gji/ggw236.

Marfurt, K. J., 1984, Accuracy of finite-difference and finite-element modeling of the scalar and elastic wave equations: Geophysics, **49**, 533–549, doi: 10.1190/1.1441689.

Muyzert, E., 2007, Seabed property estimation from ambient-noise recordings. Part 2: Scholte-wave spectral-ratio inversion: Geophysics, **72**, no. 4, U47–U53, doi: 10.1190/1.2719062.

Nolet, G., R. Sleeman, V. Nijhof, and B. L. N. Kennett, 1989, Synthetic reflection seismograms in three dimensions by a locked-mode approximation: Geophysics, **54**, 350–358, doi: 10.1190/1.1442660.

Paige, C. C., and M. A. Saunders, 1982, LSQR: An Algorithm for Sparse Linear Equations And Sparse Least Squares: Association for Computing Machinery Transactions on Mathematical Software, **8**, 43–71, doi: 10.1145/355984.355989.

Rodi, W. L., P. Glover, T. M. C. Li, and S. S. Alexander, 1975, A fast, accurate method for computing group-velocity partial derivatives for Rayleigh and Love modes: Bulletin of the Seismological Society of America, **65**, 1105–1114.

Saccorotti, G., B. Chouet, and P. Dawson, 2003, Shallow-velocity models at the Kilauea Volcano, Hawaii, determined from array analysis of tremor wavefields: Geophysical Journal International, **152**, 633–648, doi: 10.1046/j.1365-246X.2003.01867.x.

Saito, M., 1988, Disper80, *in* D. J. Doornbos, ed., Seismological algorithms: Computational methods and computer programs: Academic Press, 293–319.

Snieder, R., and J. Trampert, 1999, Inverse problems in geophysics, *in* A. Wirgin, ed., Wavefield inversion: Springer Verlag, 119–190.

Strick, E., and A. S. Ginzbarg, 1956, Stoneley-wave velocities for a fluid-solid interface: Bulletin of the Seismological Society of America, **46**, 281–292.

Takeuchi, H. M., and M. Saito, 1972, Seismic surface waves, *in* B. A. Bolt, ed., Methods in computational physics: Academic Press, 217–295.

Tarantola, A., and B. Valette, 1982, Generalized nonlinear inverse problems solved using the least squares criterion: Reviews of Geophysics and Space Physics, **20**, 219–232, doi: 10.1029/RG020i002p00219.

Tsai, V. C., and S. Atiganyanun, 2014, Green's functions for surface waves in a generic velocity structure: Bulletin of the Seismological Society of America, **104**, 2573–2578, doi: 10.1785/0120140121.

Tsai, V. C., B. Minchew, M. P. Lamb, and J.-P. Ampuero, 2012, A physical model for seismic noise generation from sediment transport in rivers: Geophysical Research Letters, **39**, L02404, doi: 10.1029/2011GL050255.

Wiggins, R. A., 1976, A fast, new computational algorithm for free oscillations and surface waves: Geophysical Journal of the Royal Astronomical Society, **47**, 135–150, doi: 10.1111/j.1365-246X.1976.tb01266.x.

Xia, J., R. D. Miller, and C. B. Park, 1999, Estimation of near-surface shear-wave velocity by inversion of Rayleigh waves: Geophysics, **64**, 691–700, doi: 10.1190/1.1444578.